Densification, Microstructure, and Wear Property of *In Situ* Titanium Nitride-Reinforced Titanium Silicide Matrix Composites Prepared by a Novel Selective Laser Melting Process

DONGDONG GU, CHEN HONG, and GUANGBIN MENG

This work presents the densification behavior, microstructural features, microhardness, and wear property of *in situ* TiN/Ti$_5$Si$_3$ composite parts prepared by a novel Selective Laser Melting (SLM) process. The occurrence of balling phenomenon at a low laser energy density combined with a high scan speed and the formation of thermal cracks at an excessive laser energy input generally decreased densification rate. The *in situ*-formed TiN reinforcing phase experienced a successive morphological change: an irregular polyangular shape—a refined near-round shape—a coarsened dendritic shape, as the applied laser energy density increased. The variations in liquid-solid wettability and intensity of Marangoni convection within laser molten pool accounted for the different growth mechanisms of TiN reinforcement. The TiN/Ti$_5$Si$_3$ composite parts prepared under the optimal SLM conditions had a near-full 97.7 pct theoretical density and a uniform microhardness distribution with a significantly increased average value of 1358.0HV$_{0.3}$. The dry sliding wear tests revealed that a considerably low friction coefficient of 0.19 without any apparent fluctuation and a reduced wear rate of 6.84×10^{-5}mm^3/Nm were achieved. The enhanced wear resistance was attributed to the formation of adherent strain-hardened tribolayer covered on the worn surface.

I. INTRODUCTION

THE titanium silicide Ti$_5$Si$_3$ intermetallic compound has been considered recently as a promising candidate material for high-temperature structural applications because of its high melting temperature [2403 K (2130 °C)], relatively low density (4.32 g/cm^3), capacity to retain high strength up to 1473 K (1200 °C), and excellent oxidation and creep resistance.[1,2] Nevertheless, because of its complex hexagonal crystal structure with a low symmetry (D8$_8$), the monolithic Ti$_5$Si$_3$ has a considerably low fracture toughness at ambient temperature.[3] Thus, a major challenge for a successful application of Ti$_5$Si$_3$ material is to reduce its room-temperature brittleness. In this respect, the existing work by Wang *et al.*,[4] Shon *et al.*,[5] and Li *et al.*[6] ascertained that the preparation of ceramic-reinforced Ti$_5$Si$_3$-based composites by incorporating the stiffer ceramic phase within Ti$_5$Si$_3$ matrix is an important method to improve the integrated mechanical properties including fracture toughness. In particular, the development of novel *in situ* composites, in which the ceramic reinforcements are synthesized in the metallic matrix by chemical reactions between elements, exhibits more significant advantages, *e.g.*, the refined microstructural scale of *in situ* formed reinforcements, the clean reinforcement/matrix interfaces with stronger interfacial bonding, and the increased thermodynamic stability and mechanical properties of the composites.[7] In contrast, a reasonable selection of the ceramic reinforcement that is feasible for Ti$_5$Si$_3$ matrix is required. It is known that the coefficient of thermal expansion (CTE) and the elastic modulus are two most important material properties that determine the level of residual stress in composites.[8] Based on the previous studies,[1,2,9] the TiC has been demonstrated to be a suitable candidate material used as the reinforcement for Ti$_5$Si$_3$-based composites because of the similar CTEs (Ti$_5$Si$_3$ 9.7×10^{-7}/K *vs* TiC 7.7×10^{-7}/K). The TiN, which has almost the same CTE (9.4×10^{-7}/K) as that of Ti$_5$Si$_3$, matches even better with Ti$_5$Si$_3$ matrix. Furthermore, the elastic modulus of TiN (250.37 GPa) is considerably lower than that of TiC (439.43 GPa),[10] and normally, the stress of composites can be controlled by using material with a low elastic modulus.[8] Therefore, the TiN can be regarded as a more promising ceramic reinforcement for Ti$_5$Si$_3$.

Bulk-form composites containing the *in situ* formed reinforcements normally are prepared by conventional methods including powder metallurgy (PM),[11,12] self-propagating high-temperature synthesis,[13–15] and casting.[16,17] However, the production of composites by

DONGDONG GU, Professor and Alexander von Humboldt Research Fellow, is with the College of Materials Science and Technology, Nanjing University of Aeronautics and Astronautics, 210016 Nanjing, People's Republic of China, and is also with the Fraunhofer Institute for Laser Technology ILT/Chair for Laser Technology LLT, RWTH Aachen, D-52074 Aachen, Germany. Contact e-mail: dongdonggu@nuaa.edu.cn CHEN HONG, PhD Candidate, is with the Fraunhofer Institute for Laser Technology ILT/Chair for Laser Technology LLT, RWTH Aachen. GUANGBIN MENG, Graduate Student, is with the College of Materials Science and Technology, Nanjing University of Aeronautics and Astronautics.

these conventional processes is prone to generate large agglomerates of reinforcing phases, thereby decreasing the microstructural homogeneity and resultant mechanical properties. Furthermore, the high-temperature ceramic reinforcing phases typically remain in particle morphology in the conventional composites because the workable processing temperature normally cannot increase above the melting points of ceramics. The incorporation of the solid ceramic particles within the matrix, however, tends to induce the formation of interfacial microcracks because of the limited wetting characteristics between ceramics and metals. In contrast, the conventional processes, which generally need expensive and dedicated tools such as molds or dies, are not suitable for small-volume production and complex shapes. The complicated preprocessing and postprocessing steps necessary in conventional routes make them a time-consuming process. The probability of the formation of process defects also increases during the long cycle time. Therefore, novel processing methods are highly required for the direct net-shape fabrication of complex-shaped ceramic reinforced composite components with favorable microstructural and mechanical properties.

Selective laser melting (SLM), as a newly developed rapid prototyping (RP) technique,[18–22] has the capability to fabricate three-dimensional parts with any complex configurations directly from powder materials.[23–26] SLM creates fully dense parts in a layer-by-layer manner by selectively fusing and consolidating thin layers of loose powder using a high-energy laser beam, without any postprocessing requirements. Recently, some preliminary research[27,28] focused on the preparation of in situ composite parts using the SLM process, considering its flexibility in feedstock and shapes. Nevertheless, because of the complex metallurgical nature of in situ SLM system, which involves both chemical reactions and multiple modes of heat, mass, and momentum transfer, SLM-processed composites may suffer from processing problems such as gas entrapment, aggregation of reinforcements, residual stresses, and interfacial microcracks. Furthermore, SLM is performed based on a complete melting/solidification mechanism, and accordingly, the high-melting-point ceramic reinforcing phases are formed through a dissolution/precipitation manner. Different to the particle morphology before melting, the in situ formed ceramic crystals may have versatile growth morphologies in the finally solidified structures. Therefore, the unpredictability and/or uncontrollability of the formation of in situ phases and microstructures in a SLM route are still a major challenge. As the microstructural features of laser-processed powder may influence the attendant mechanical properties significantly, a detailed understanding of the crystallization mechanism and microstructural development of the in situ phases is required.

In the current work, SLM of Si_3N_4/Ti powder system was performed to prepare bulk-form TiN/Ti_5Si_3 in situ composites. The evolutions of phases and microstructures of SLM-processed composites under different laser processing parameters were studied and the mechanical properties such as densification rate, microhardness, and wear property were assessed. The predominant metallurgical mechanisms responsible for the variations in microstructural and mechanical properties were disclosed.

II. EXPERIMENTAL PROCEDURE

A. Powder Preparation

The 99.9 pct purity Ti powder with a polyangular structure and an average particle size of 30 μm and the 99.5 pct purity Si_3N_4 powder with an irregular shape and a mean particle size of 4 μm were used as the starting materials. According to the Si_3N_4:Ti weight ratio of 24.55:75.45 (i.e., the equivalent mol ratio of 1:9), the two components were milled using a high-energy Pulverisette 6 planetary mono-mill (Fritsch GmbH, Idar-Oberstein, Germany). Stainless steel grinding balls and the powder mixture to be treated were charged into the grinding bowl, with the ball-to-powder weight ratio of 10:1. High-purity argon was used as the protective gas. The milling time and the rotation speed of the main disk were settled at 8 hours and 250 rpm, respectively. To avoid the excessive temperature increase within the grinding bowl, ball milling duration of 20 minutes was followed by an interval of 10 minutes. Details concerning powder preparation have been addressed in the literature.[29] The as-milled composite powder had a near-spherical shape and a refined particle size of 8 to 22 μm.

B. Laser Processing

The SLM apparatus, as illustrated schematically in Figure 1(a), consisted mainly of a 2000 SM continuous wave Gaussian CO_2 laser (λ = 10.6 μm) with a maximum output power of 5 kW and a focused spot size at the substrate surface of 0.3 mm (Rofin-Sinar Laser GmbH, Hamburg, Germany), an automatic powder layering system with a roller, a computer system for process control, and an inert argon gas protection system. As the parts were to be prepared, a titanium substrate was placed primarily on the building platform and leveled. A thin layer of the milled powder (0.1 mm in thickness) was then deposited on the substrate by the roller. Subsequently, the laser beam scanned the powder bed surface to form layer-wise profiles according to the computer-aided design data of the parts. A simple linear raster scan pattern was used (Figure 1(b)) with a scan line spacing of 0.15 mm. The similar process was repeated in a layer-by-layer manner until multilayer parts with dimensions of 8 mm $\times$ 8 mm $\times$ 6 mm were finished. Through a series of preliminary SLM experiments, the laser power was optimized at 1 kW. Meanwhile, the scan speeds were settled periodically at 0.1, 0.2, 0.3, and 0.4 m/s by the SLM control program. Four different "linear laser energy densities" (η) of 10, 5, 3.33, and 2.5 kJ/m, which was defined by the ratio of laser power to scan speed,[30] were used to estimate the laser energy input to the powder layer being treated.
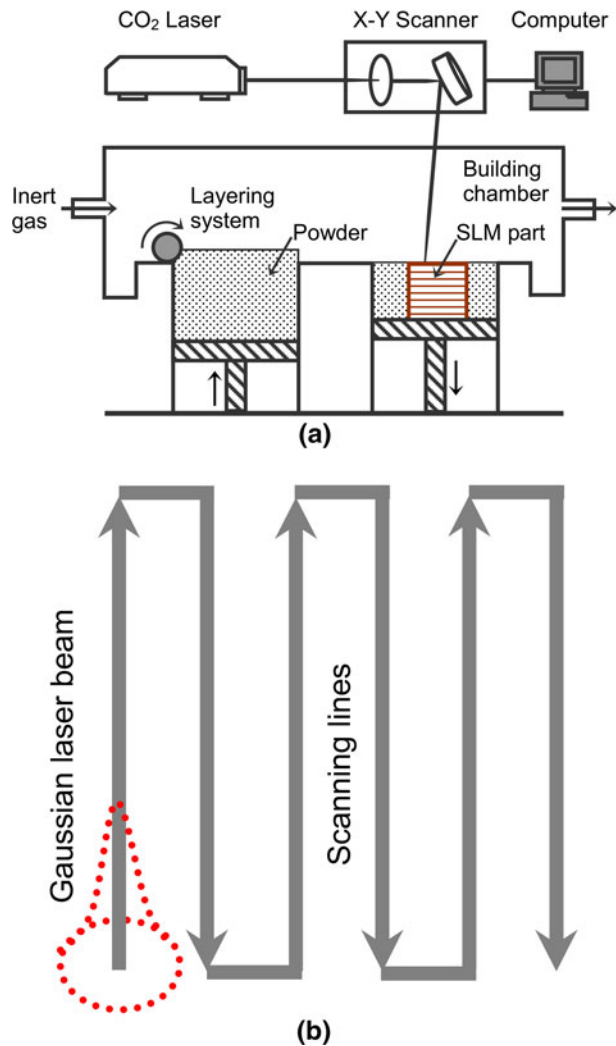
Fig. 1—Schematics of SLM apparatus (*a*) and laser scanning pattern (*b*).

C. *Microstructural Characterization*

Phase identification was performed by a D8 Advance X-ray diffractometer (XRD) (Bruker AXS GmbH, Germany) with Cu Kα radiation at 40 kV and 40 mA, using a continuous scan mode. A quick scan at 4 deg/min was performed primarily over a wide range of $2\theta = 30$ to 80 deg. A slower scan rate of 1 deg/min was used over $2\theta = 34.0$ to 36.0 deg and $2\theta = 39.0$ to 41.0 deg to give a more accurate determination of diffraction peaks. Samples for metallographic examinations were cut, ground, and polished according to standard procedures and were etched with a solution consisting of HF (4 mL), HNO_3 (6 mL), and distilled water (100 mL) for 45 seconds. The microstructures were characterized using a Quanta 200 scanning electron microscope (SEM) (FEI Company, Hillsboro, OR) in a secondary electron mode at an accelerating voltage of 20 kV. A UTHSCSA ImageTool 3.0 image processing and analysis program was used to acquire the sizes of reinforcing particles. Chemical compositions were determined by an EDAX Genesis energy dispersive X-ray (EDX) spectroscope (EDAX Inc., Mahwah, NJ), using a super-ultra thin window sapphire detector.

D. *Mechanical Properties Testing*

The density (ρ) of SLM-processed samples was measured based on the Archimedes principle. The Vickers hardness was determined using a MicroMet 5101 microhardness tester (Buehler GmbH, Düsseldorf, Germany) at a load of 0.3 kg and an indentation time of 15 seconds. Dry sliding wear tests were conducted in a HT-500 ball-on-disk tribometer (Lanzhou ZhongKe KaiHua Sci. & Technol. Co., Ltd., Lanzhou, China) in air at room temperature. The surfaces of the specimens were ground and polished prior to wear tests. A bearing steel GCr15 ball with a diameter of 3 mm and a mean hardness of HRC60 was taken as the counterface material and a test load of 3N was applied. The friction unit was rotated at a speed of 560 rpm for 30 minutes and the rotation radius was fixed at 2 mm. The friction coefficients of the specimens were recorded during wear tests. The wear volume (V) was determined gravimetrically using $V = M_{loss}/\rho$, where M_{loss} was the weight loss of the specimens after wear tests. The wear rate (ω) was calculated by $\omega = V/(WL)$, where W was the contact load and L was the sliding distance.

III. RESULTS AND DISCUSSION

A. *Phases*

Figure 2 depicted the typical XRD patterns of SLM-processed composite parts. The strong diffraction peaks corresponding to TiN (based on JCPDS Card No. 87-0632) and Ti_5Si_3 (based on JCPDS Card No. 29-1362) phases were generally identified in SLM-processed parts at different laser energy input. To reveal the reaction behaviors of the Si_3N_4 and Ti constituents in the starting composite powder, a more accurate XRD scan at a relatively low rate was performed in the vicinity of the strongest diffraction peaks of Si_3N_4 ($2\theta = 35.344$ deg) and Ti ($2\theta = 40.161$ deg), as illustrated in Figure 3. It was observed that the initial Si_3N_4 and Ti diffraction peaks disappeared completely in all SLM-processed parts. Therefore, it was reasonable to conclude that for the given laser energy densities of 2.5 to 10 kJ/m, SLM processing of Si_3N_4/Ti powder system generally led to the *in situ* formation of TiN/Ti_5Si_3 composites free of any residual impurity phases.

When the high-energy laser beam scans over the powder layer, the energy is absorbed directly by the powder through both bulk coupling and powder coupling mechanisms,[31] thereby realizing the thermalization of the absorbed laser energy. The Si_3N_4/Ti powder particles are heated up speedily, typically within a considerably short timescale below 4 ms,[32] leading to the complete melting of Ti constituent as the operative temperature reaches its melting point [~1943 K (1670 °C)]. Because of a considerably high thermalization caused by high-energy laser irradiation coupled with the sufficient wetting of Ti liquid in the molten
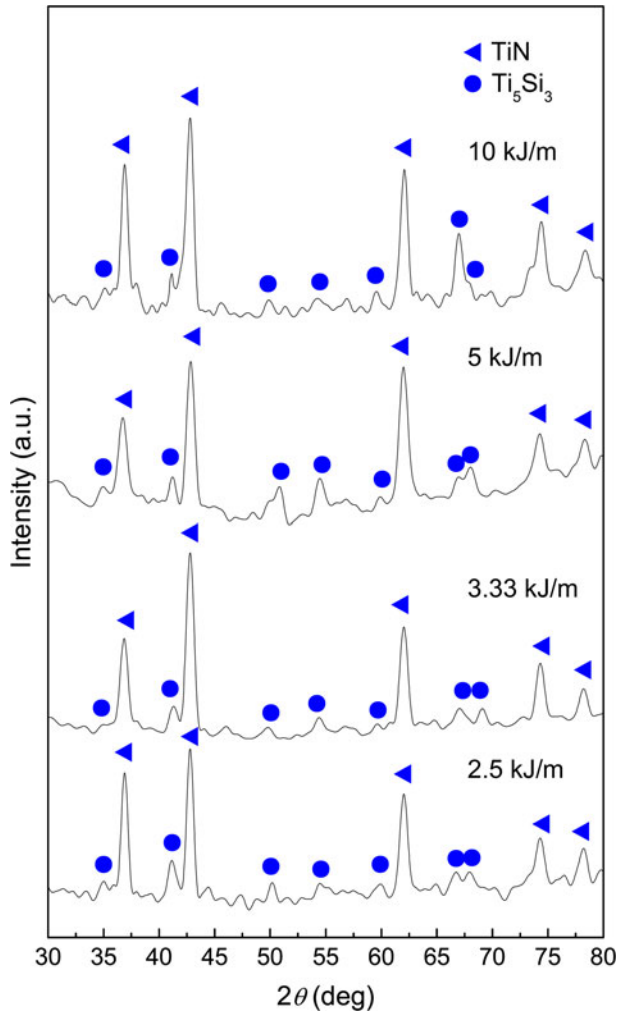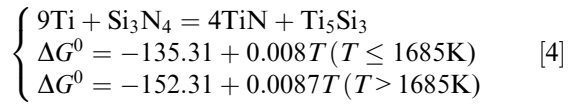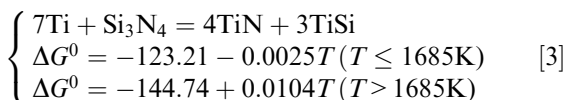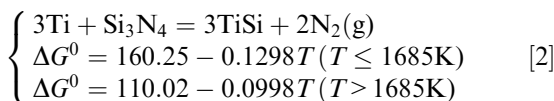
Fig. 2—XRD spectra of SLM-processed composite parts at different laser energy densities.

$$\begin{cases} 9Ti + Si_3N_4 = 4TiN + Ti_5Si_3 \\ \Delta G^0 = -135.31 + 0.008T \, (T \leq 1685K) \\ \Delta G^0 = -152.31 + 0.0087T \, (T > 1685K) \end{cases} \quad [4]$$

A thermodynamic analysis, as presented in Figure 4, reveals that when temperature reaches above 1700 K, reaction [4] is much easier to proceed than others because the ΔG^0 of this reaction is in a minimal negative value. SLM of the Si_3N_4/Ti powder system implies that a complete melting mechanism is involved. The operative temperature, thus, approaches or even exceeds 2173 K (1900 °C), favoring the initiation of *in situ* reaction [4] as the starting Si_3N_4/Ti molar ratio of 1:9 is settled. Furthermore, according to Reference 34, the change in the enthalpy (ΔH) of reaction [4] is -912.912 kJ/mol. A small, negative ΔH implies an exothermic nature of the system, which can act as the driving force for the reaction.

B. Microstructures and Compositions

The characteristic microstructures on the etched cross-sections of SLM-processed composite parts were provided in Figure 5. EDX point scans were performed, respectively, on the reinforcement and the matrix to determine the elemental distributions. The reinforcing phase (point A) was composed of the Ti and N elements with a near-equal atomic proportion (Figure 5(e)). The Ti and Si elements were detected within the matrix (point B), in which the Ti:Si atomic ratio was close to 5:3 (Figure 5(f)). Combined with the XRD (Figure 2) and EDX (Figure 5(e) and (f)) results, it was confirmed that the *in situ* TiN-reinforced Ti_5Si_3 matrix composites were prepared successfully by SLM of the Si_3N_4/Ti powder system. Nevertheless, the microstructural features of the *in situ* presented TiN reinforcing phase (*e.g.*, shape, size, and dispersion state) exhibited distinct changes with the applied laser-processing parameters. At a relatively low η of 2.5 kJ/m, the TiN reinforcing phase exhibited a nonuniform polyangular structure and a certain degree of agglomeration (Figure 5(a)), having a relatively large average particle size of 11.7 μm (Figure 6). As η increased to 3.33 kJ/m, the surface of the TiN-reinforcing phase showed an apparent smoothening (Figure 5(b)), although the mean particle size remained almost unchanged at 11.0 μm (Figure 6). Interestingly, at a higher η of 5 kJ/m, the TiN reinforcement had a refined granular morphology with a significantly reduced size of 6.5 μm (Figure 6) and, meanwhile, distributed homogeneously throughout the matrix (Figure 5(c)). In this instance, the TiN particles exhibited a smooth and near-round shape, with a clear and coherent reinforcement/matrix interface free of any interfacial microcracks (Figure 5(g)). On further enhancing the applied η to 10 kJ/m, the growth morphology of TiN reinforcement changed considerably; it developed into an entirely different dendritic structure (Figure 5(d)). However, the TiN dendrites showed a large degree of coarsening, reaching a considerably large particle size of 18.3 μm (Figure 6).

As stated previously, SLM is performed based on a complete melting/solidification mechanism, and accordingly,

pool, the Si_3N_4 constituent having a slightly higher decomposition point of ~2173 K (1900 °C) tends to decompose to releases atomic Si and N. An *in situ* reaction system consisting of a ternary Ti–Si–N melt is, thus, generated. It is known that there are several possible chemical reactions for the Si_3N_4/Ti system during high-temperature processing, depending on the initial component ratios. The dependence of the standard Gibbs free energy (ΔG^0, kJ/mol) of these reactions on the temperature (T, K) is as follows[33]:

$$\begin{cases} 5Ti + Si_3N_4 = Ti_5Si_3 + 2N_2(g) \\ \Delta G^0 = 25.07 - 0.06T \, (T \leq 1685K) \\ \Delta G^0 = -5.07 - 0.042T \, (T > 1685K) \end{cases} \quad [1]$$

$$\begin{cases} 3Ti + Si_3N_4 = 3TiSi + 2N_2(g) \\ \Delta G^0 = 160.25 - 0.1298T \, (T \leq 1685K) \\ \Delta G^0 = 110.02 - 0.0998T \, (T > 1685K) \end{cases} \quad [2]$$

$$\begin{cases} 7Ti + Si_3N_4 = 4TiN + 3TiSi \\ \Delta G^0 = -123.21 - 0.0025T \, (T \leq 1685K) \\ \Delta G^0 = -144.74 + 0.0104T \, (T > 1685K) \end{cases} \quad [3]$$
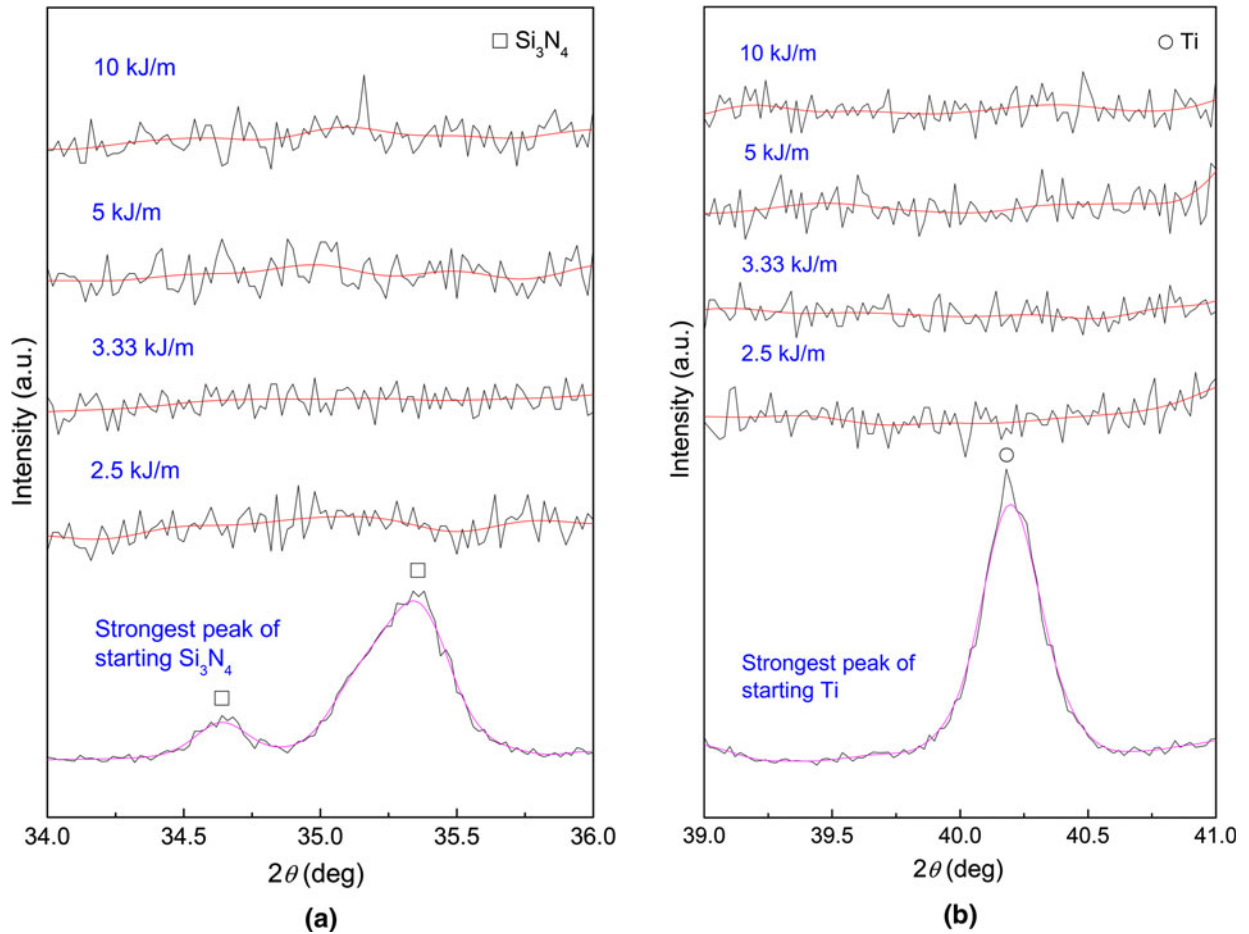
Fig. 3—XRD spectra in the vicinity of the strongest diffraction peaks of starting Si_3N_4 (a) and Ti (b) phases showing the complete exhaustion of constituents after SLM. The underlying relatively smooth spectra are obtained by XRD scan at a faster rate.
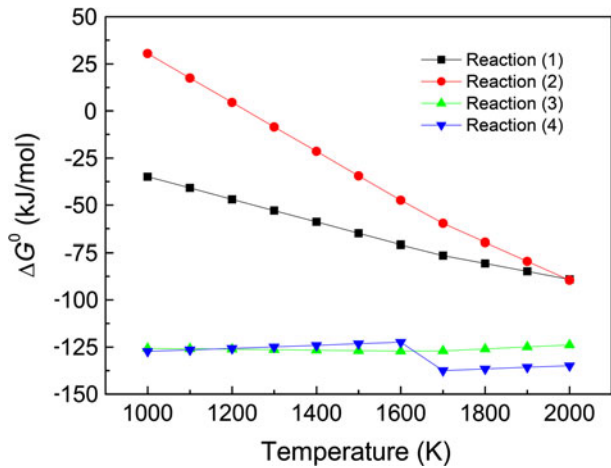

Fig. 4—Relation between standard Gibbs free energy and temperature for various reactions of Si_3N_4/Ti system.

the TiN-reinforcing phase is formed through a dissolution/precipitation mechanism by means of the heterogeneous nucleation of TiN nuclei from the ternary Ti–Si–N melt and subsequent grain growth.[35] The previous studies on the conventional PM-processed Ti–Si based *in situ* composites indicate that the ceramic reinforcement is

typically in a particle morphology[4–6,13] because of a solid-state sintering or a partially melted liquid phase sintering mechanism applied. Differently, the *in situ* TiN reinforcing phase in SLM-processed TiN/Ti_5Si_3 composites experiences an interesting change in its morphologies from an irregular polyangular shape to a refined near-round shape and, finally, to a coarsened dendritic shape, on increasing the applied laser energy density (Figures 5(a) through (d)). During SLM, the local temperature gradient and chemical concentration gradient in the molten pool give rise to surface tension gradient and associated Marangoni convection.[30,32] The formation of convective stream within the pool induces liquid capillary force, which subsequently exerts on the precipitated solid-state TiN nuclei by the wetting liquid around. The intensity of Marangoni flow can be estimated using the dimensionless Marangoni number (M_a)[36]:

$$M_a = \frac{\Delta \sigma L}{\mu v_k} \quad [5]$$

where $\Delta \sigma$ is the surface tension difference of Marangoni flow, L the length of the free surface, μ the dynamic viscosity, and v_k is the kinematic viscosity. The wetting property of the *in situ* precipitated reinforcing phase by
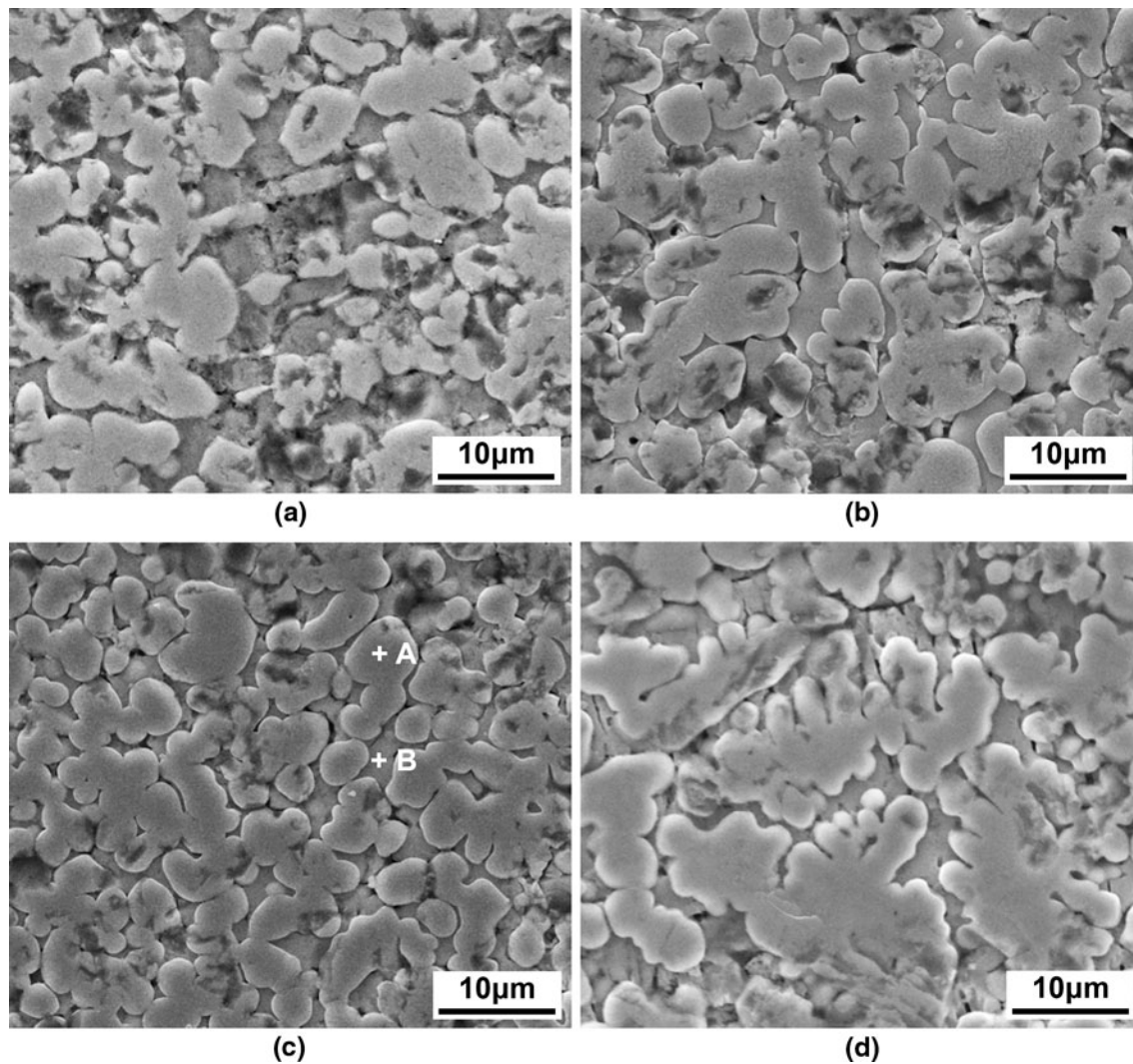
Fig. 5—SEM images showing characteristic microstructures of SLM-processed composite parts at various scan speeds (v) and laser energy densities (η): (a) $v = 0.4$ m/s, $\eta = 2.5$ kJ/m; (b) $v = 0.3$ m/s, $\eta = 3.33$ kJ/m; (c) $v = 0.2$ m/s, $\eta = 5$ kJ/m; (d) $v = 0.1$ m/s, $\eta = 10$ kJ/m. EDX analyses showing chemical compositions collected in point A (e) and point B (f). High-magnification micrograph showing interfacial microstructure of composites prepared at $\eta = 5$ kJ/m (g).

the liquid is crucial in determining its final morphology and dispersion state. Based on Zhou *et al.*'s results,[37] for a reactive wetting system of liquid metal on ceramic phase, the wettability is predominated by the formation of ceramic phase during processing. The equilibrium contact angle θ_{eq} can be approximately expressed as

$$\cos \theta_{eq} = (\gamma_{sv} - \gamma_{ls})/\gamma_{lv} \qquad [6]$$

where γ_{lv}, γ_{sv}, and γ_{ls} are the interface tensions of liquid metal-vapor, reacted ceramic-vapor, and liquid metal-reacted ceramic, respectively. For the Ti–Si liquid system, γ_{ls} is controlled by the temperature T and can be estimated by[38]

$$\gamma_{ls} = 1656 - 0.375T \qquad [7]$$

A proper increase in the applied η from 2.5 kJ/m to 5 kJ/m tends to increase the workable T, which in turn lowers γ_{ls} (Eq. [7]). Therefore, a lower contact angle θ_{eq} (Eq. [6]) and, accordingly, an increased liquid–solid

wetting property are achieved. The *in situ* synthesized TiN-reinforcing phase, therefore, tends to undergo a sufficient wetting by the surrounding liquid, leading to a pronounced smoothening and refinement of the initial polyangular TiN precipitates (Figure 5(a) and (c), Figure 7). In contrast, as revealed in Eq. [5], M_a is inversely proportional to μ, which can be further defined by[39]

$$\mu = \frac{16}{15} \sqrt{\frac{m}{kT}} \gamma_{ls} \qquad [8]$$

where m is the atomic mass and k is the Boltzmann constant. When a considerably high η of 10 kJ/m is used for SLM, the resultant higher T and lower γ_{ls} (Eq. [7]) both result in a significant decrease in μ (Eq. [8]), hence intensifying the Marangoni flow and attendant turbulence within the molten pool (Eq. [5]). Because of the instability of the solid–liquid interface caused by the perturbation, the *in situ* TiN precipitates tend to
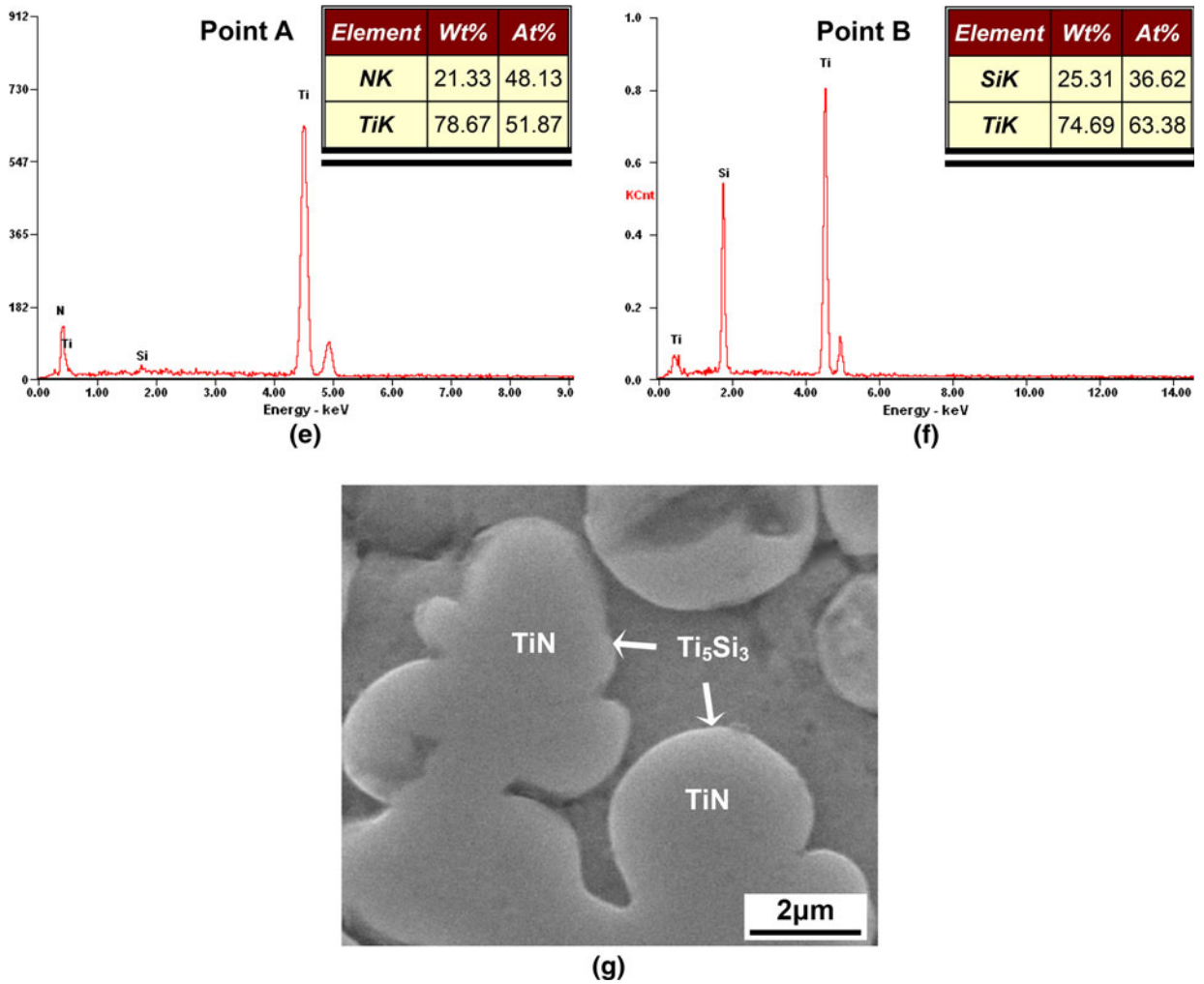
Point A

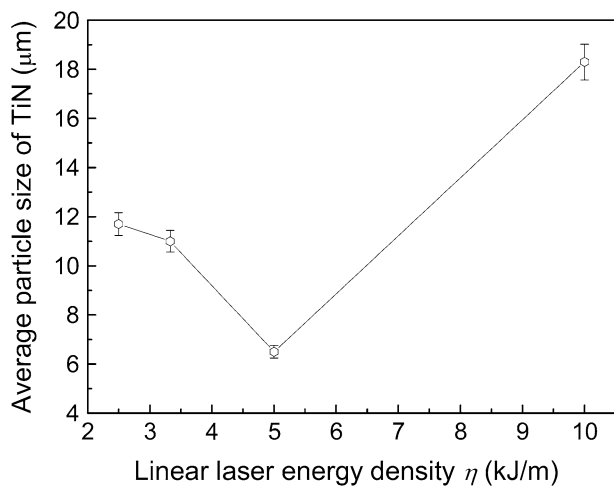| Element	Wt%	At%
NK	21.33	48.13
TiK	78.67	51.87

(e)

Point B

Element	Wt%	At%
SiK	25.31	36.62
TiK	74.69	63.38

(f)

(g)

Fig. 5—Continued.

Fig. 6—Change of the mean particle size of TiN reinforcing phase with the applied laser energy density.

Fig. 7—Schematic of growth mechanisms and morphologies of *in situ* TiN-reinforcing phase from the liquid under laser beam irradiation.

experience a dendrite growth (Figure 7). Furthermore, because of a markedly increased thermalization of laser energy in this 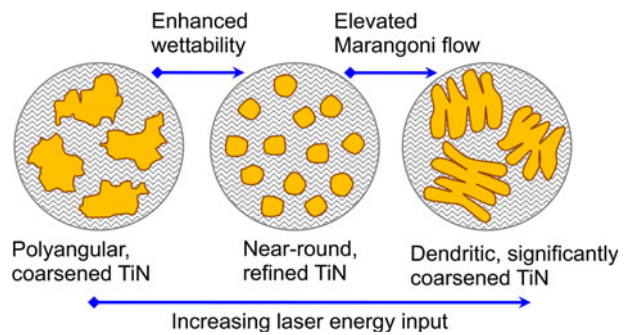instance, a large amount of heat is accumulated around the growing dendrite tips, thereby offering significant internal energy and thermodynamic potentials for the coarsening of the finally developed TiN dendrites (Figure 5(d)).

It is worth noting that in our current study, there is no apparent change in the microstructures along the layer-by-layer deposition direction inside the SLM-processed composite parts. Unlike the RP method based on a

semisolid mechanism, *e.g.*, direct metal laser sinter-ing,[30,32] the SLM process is performed based on a complete melting metallurgical mechanism. In other words, each layer is consolidated through the complete melting/solidification manner. Although to some extent, the surface of the previously processed layer will remelt as the subsequent layer is processed, such a remelting cannot lead to a substantial change of the previously melted/solidified microstructures.

C. *Densification Behavior*

Figure 8 showed the typical surface morphologies of SLM-processed parts under various processing condi-tions. The obtained relative densities of the correspond-ing parts were depicted in Figure 9. At a relatively high *v* combined with a low *η*, a considerably rough surface consisting of a large amount of small-sized spherical balls with an average diameter of ~20 μm was formed (Figure 8(a)). Also, narrow microcracks, as indicated selectively in Figure 8(a), were observed on laser-pro-cessed surface. The combined influence of these two

defects resulted in a limited densification level of 86.3 pct theoretical density (TD) (Figure 9). On increas-ing *η* by decreasing the applied *v*, the balling phenom-enon was alleviated, although the residual open porosity was still present on the surface (Figure 8(b)). In this situation, the SLM densification response, 89.5 pct TD, still remained insufficient (Figure 9). As a *η* of 5 kJ/m was properly settled, a pretty dense surface consisting of coherently bonded scan tracks was yielded, free of any balling effect and crack formation (Figure 8(c)), achiev-ing a near-full 97.7 pct TD (Figure 9). As a considerably low *v* and attendant high *η* of 10 kJ/m were used, the surface became even smoother. However, the intercon-nected deep cracks were elongated on SLM-processed surface, almost perpendicular to the building direction. The length of cracks was on the order of 1 mm and the width was ~15 μm (Figure 8(d)), which decreased the densification rate to 92.4 pct TD (Figure 9).

From the parameter-dependent surface morphologies (Figure 8), one can conclude that the relatively poor densification activity at a lower or a higher *η* is due to the occurrence of balling effect (Figure 8(a)) and
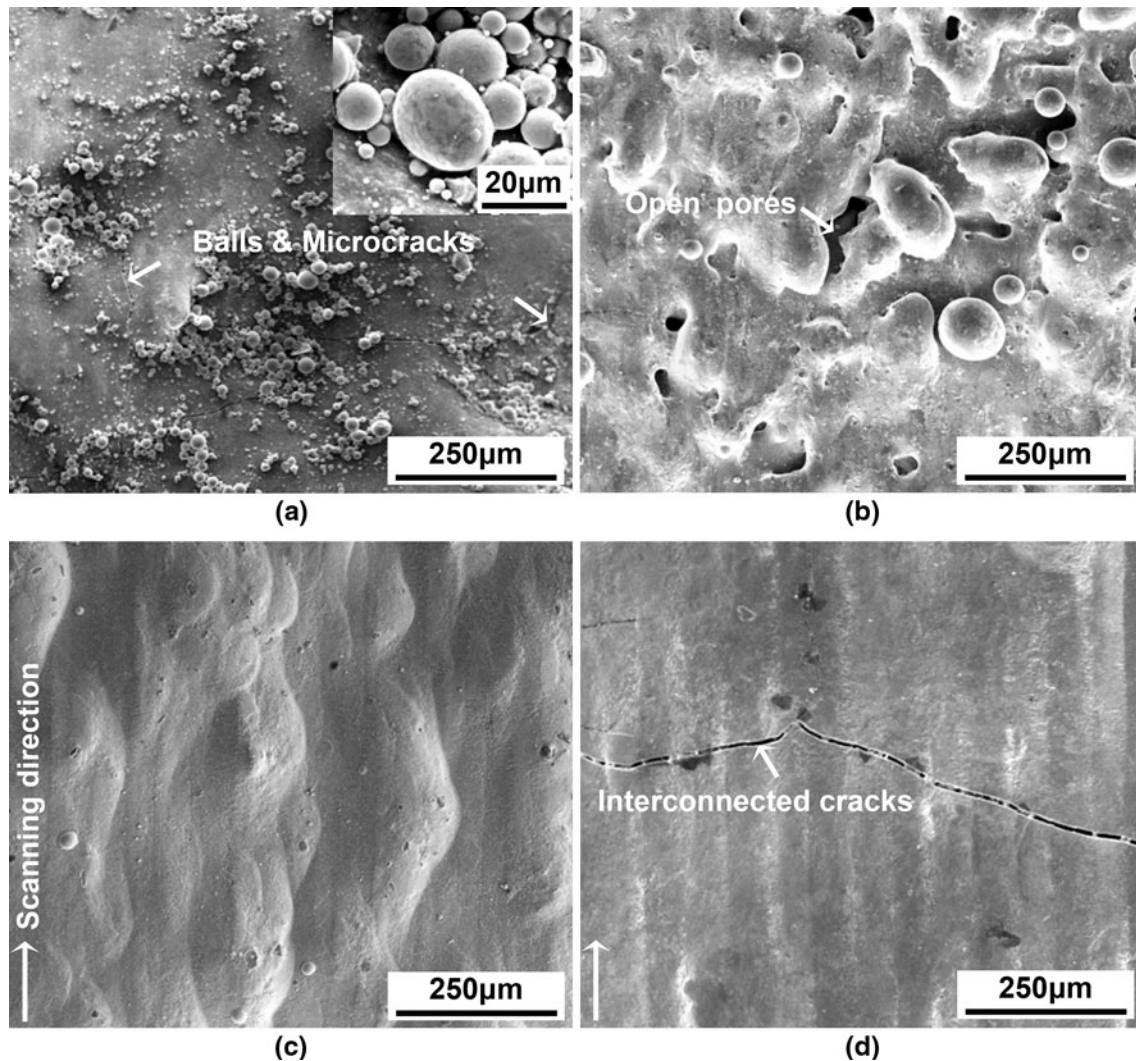

Fig. 8—SEM images showing the typical surface morphologies of SLM-processed composite parts at different scan speeds (*v*) and laser energy densities (*η*): (*a*) *v* = 0.4 m/s, *η* = 2.5 kJ/m; (*b*) *v* = 0.3 m/s, *η* = 3.33 kJ/m; (*c*) *v* = 0.2 m/s, *η* = 5 kJ/m; (*d*) *v* = 0.1 m/s, *η* = 10 kJ/m.
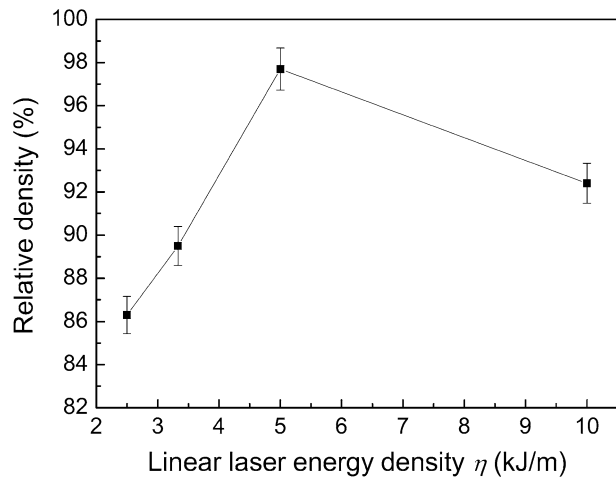
Fig. 9—Effect of laser energy density on densification rate of SLM-processed composite parts.

Fig. 10—Schematic of balling effect during SLM of composite powder using a high scan speed.

thermal cracking (Figure 8(d)), respectably. As a complete liquid system is generated during SLM, a rapid laser scanning tends to shape the melt primarily into a continuous cylindrical molten track because of a considerably short dwelling time of laser spot on each irradiating region. However, the current molten track is in a highly unstable state. The surface energy of the liquid track will keep decreasing to obtain a final equilibrium state. According to Niu and Chang's results,[40] the applied scan speed has a significant influence on the capillary instability of the liquid track. A higher scan rate and the resultant lower laser energy input may result in a rapid decrease of the radius R of the scan track at a constant laser wavelength λ, and thus an increase of λ/R. The increase of the λ/R ratio tends to cause melt instability and, accordingly, enhances the tendency for balling initiation. Under this condition, several small-sized liquid droplets tend to splash from the surface of the molten track because of the reduction in the surface energy of liquid at short length scales (Figure 10). After solidification, a large amount of micrometer-scaled spherical splashes are formed around the laser-processed surface (Figure 8(a)). A balling effect, which is regarded as a typical defect associated with SLM, tends to produce a high amount of interball residual porosity, severely degrading the densification rate of SLM-processed parts.[25] In contrast, the shrinkage rate $\mathrm{d}(\Delta L/L_0)/\mathrm{d}t$ during SLM solidification can be estimated by[41]

$$\frac{\mathrm{d}(\Delta L/L_0)}{\mathrm{d}t} = \frac{\Delta PW}{D\mu} \quad [9]$$

where ΔP is the capillary pressure, D the grain diameter, and W is the liquid thickness. As analyzed in Eq. [8], using an excessive laser energy input (10 kJ/m) produces a considerably low μ, which in turn increases the shrinkage rate during solidification (Eq. [9]). Consequently, a large amount of thermal stresses tend to generate in the solidified parts. A theoretical and experimental study by Mercelis and Kruth[42] revealed
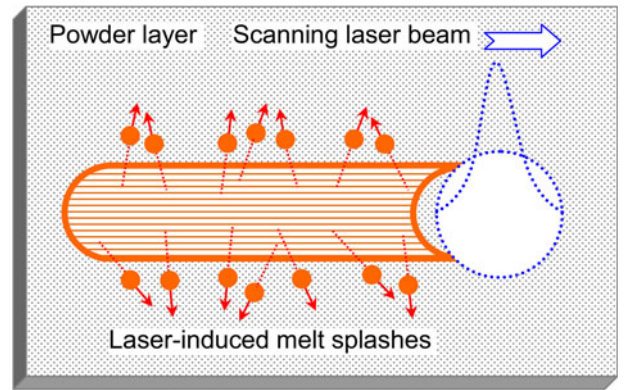
that, in general, the residual stress profile in a SLM part consists of two zones of large tensile stresses at the top and bottom of the part, and a large zone of intermediate compressive stress in between. The residual of such complicated tensile stresses on the surface results in the formation of thermal cracks and the decrease in densification response of SLM parts (Figures 8(d) and 9). Recent work by Kim et al.[43] reported the preparation of TiN-based Ti_5Si_3/TiN composites by the pyrolysis of preceramic polymer with filler. The obtained maximum density reaches 99.2 pct TD. Besides the difference in processes, the composites developed in Kim et al.'s work are TiN-based, whereas the composites in our current work are Ti_5Si_3 based. Ti_5Si_3, as an intermetallic material, is much more brittle than TiN, which will inevitably influence the final densification.

D. Microhardness and Wear Property

Figure 11(a) depicted the microhardness and its distribution measured on the cross-sections of SLM-processed composite parts. On increasing the applied η from 2.5 kJ/m to 3.33 kJ/m, the mean microhardness increased from $1083.5\mathrm{HV}_{0.3}$ to $1161.7\mathrm{HV}_{0.3}$. Nevertheless, the microhardness distribution remained a large degree of fluctuation. Differently, a uniform distribution of the microhardness with a considerably high average value of $1358.0\mathrm{HV}_{0.3}$ was achieved using a suitable η of 5 kJ/m because of the formation of homogeneously dispersed and significantly refined TiN reinforcement (Figure 5(c)). Another increase in the applied η to 10 kJ/m, however, decreased the obtained microhardness to $1264.2\mathrm{HV}_{0.3}$ and, meanwhile, intensified the fluctuation of hardness values. The coarsening of TiN dendrites and the resultant decrease in microstructural homogeneity (Figure 5(d)) were responsible for this phenomenon. For a comparison purpose, the pure Ti parts without any reinforcement were prepared using the same SLM parameters and the obtained mean microhardness was generally below $290\mathrm{HV}_{0.3}$. The microhardness of the in situ TiN/Ti_5Si_3 composites prepared by SLM of Si_3N_4/Ti system, thus, showed at least a 4-fold increase on that of the unreinforced Ti. Furthermore, based on Tsukuma et al.'s[44] and Wani et al.'s[45] work on hot
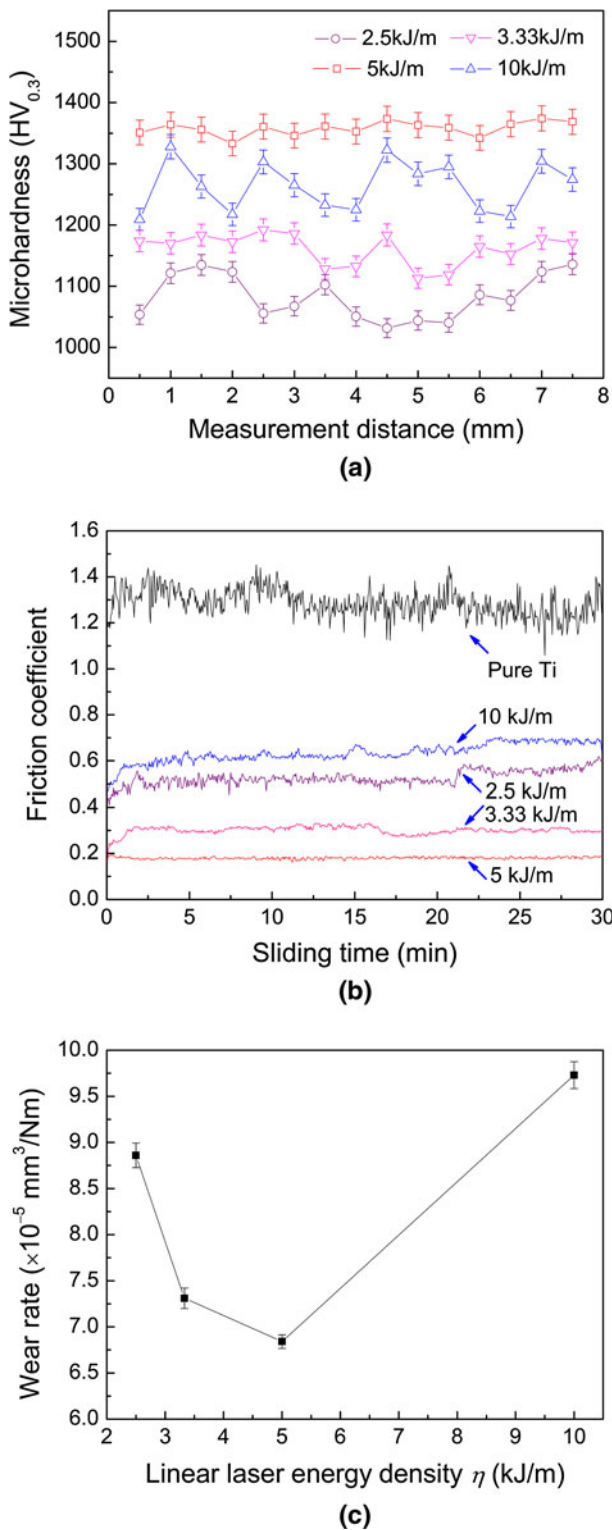
Fig. 11—Effect of laser energy density on microhardness and its distribution (a), friction coefficient (b), and wear rate (c) of the SLM-processed composite parts.

pressing of pure Si_3N_4, the obtained microhardness was approximately 1500HV. The maximum microhardness of SLM-processed *in situ* TiN/Ti_5Si_3 composites, accordingly, was close to that of Si_3N_4.

The changes of friction coefficients and wear rates of SLM-processed parts were illustrated in Figure 11(b) and (c), respectively. A comparative study revealed that the *in situ* TiN/Ti_5Si_3 composite parts generally demonstrated much lower friction coefficients than that of the unreinforced Ti part with an average value of ~1.3. Furthermore, the friction coefficients of TiN/Ti_5Si_3 parts exhibited a considerably slight local fluctuation as relative to the Ti part. A significantly enhanced wear performance of TiN/Ti_5Si_3 parts was thus ascertained. In contrast, the applied η exerted a significant influence on the wear performance of TiN/Ti_5Si_3 parts. An increase in the η from 2.5 kJ/m to 3.33 kJ/m led to a decrease in the average friction coefficient from 0.50 to 0.30 and the attendant wear rate from 8.86×10^{-5} mm³/Nm to 7.31×10^{-5} mm³/Nm. The TiN/Ti_5Si_3 part prepared at 5 kJ/m exhibited the superior wear property. A uniform distribution of friction coefficient with a considerably low mean value of 0.19 was obtained, leading to the lowest wear rate of 6.84×10^{-5} mm³/Nm. However, at an even higher η of 10 kJ/m, the average friction coefficient and wear rate of TiN/Ti_5Si_3 part increased markedly to 0.65 and 9.73×10^{-5} mm³/Nm, respectively.

To disclose the microstructural features accounting for the wear properties, the morphologies of worn surfaces were characterized in Figure 12. At a relatively low η of 2.5 kJ/m, the worn surface was considerably rough and loose, consisting of parallel grooves and granular wear debris (Figure 12(a)). Such a microstructure illustrated that the specimen suffered a severe abrasive wear, which in turn resulted in a relatively high wear rate (Figure 11(c)). As η increased to 3.33 kJ/m, a large portion of the worn surface was covered with the smooth adhesion tribolayer (Figure 12(b)). When an increased η of 5 kJ/m was settled properly, a smooth strain-hardened tribolayer was continuously sticking to the worn surface, showing no local plowing or fracturing of the surface (Figure 12(c)). During wear tests, the counterface ball slid against the surface continuously. The worn surface experienced the sufficient plastic deformation at a temperature below its recrystallization temperature. The material strengthening, thus, occurred because of the dislocation movements within the crystal structure of the material, typically in the sliding-treated layer, which was known as strain-hardened tribolayer.[46] It was believed that the *in situ* homogeneous and refined TiN reinforcement (Figure 5(c)) was not easy to split during sliding but had a high tendency to adhere to each other and get strain-hardened, favoring the complete formation of tribolayer to enhance wear resistance. However, the severely fragmented tribolayer, deep cracks, and large debris were observed on the worn surface of SLM-processed TiN/Ti_5Si_3 part at 10 kJ/m (Figure 12(d)). The resultant wear rate showed an approximately 1.5-fold increase on that of the TiN/Ti_5Si_3 part prepared at 5 kJ/m (Figure 11(c)). The poor densification caused by thermal cracking (Figure 8(d)) and the significant coarsening of the dendritic TiN reinforcement (Figure 5(d)) might account for the spalling of tribolayer and, accordingly, the decrease in wear property.
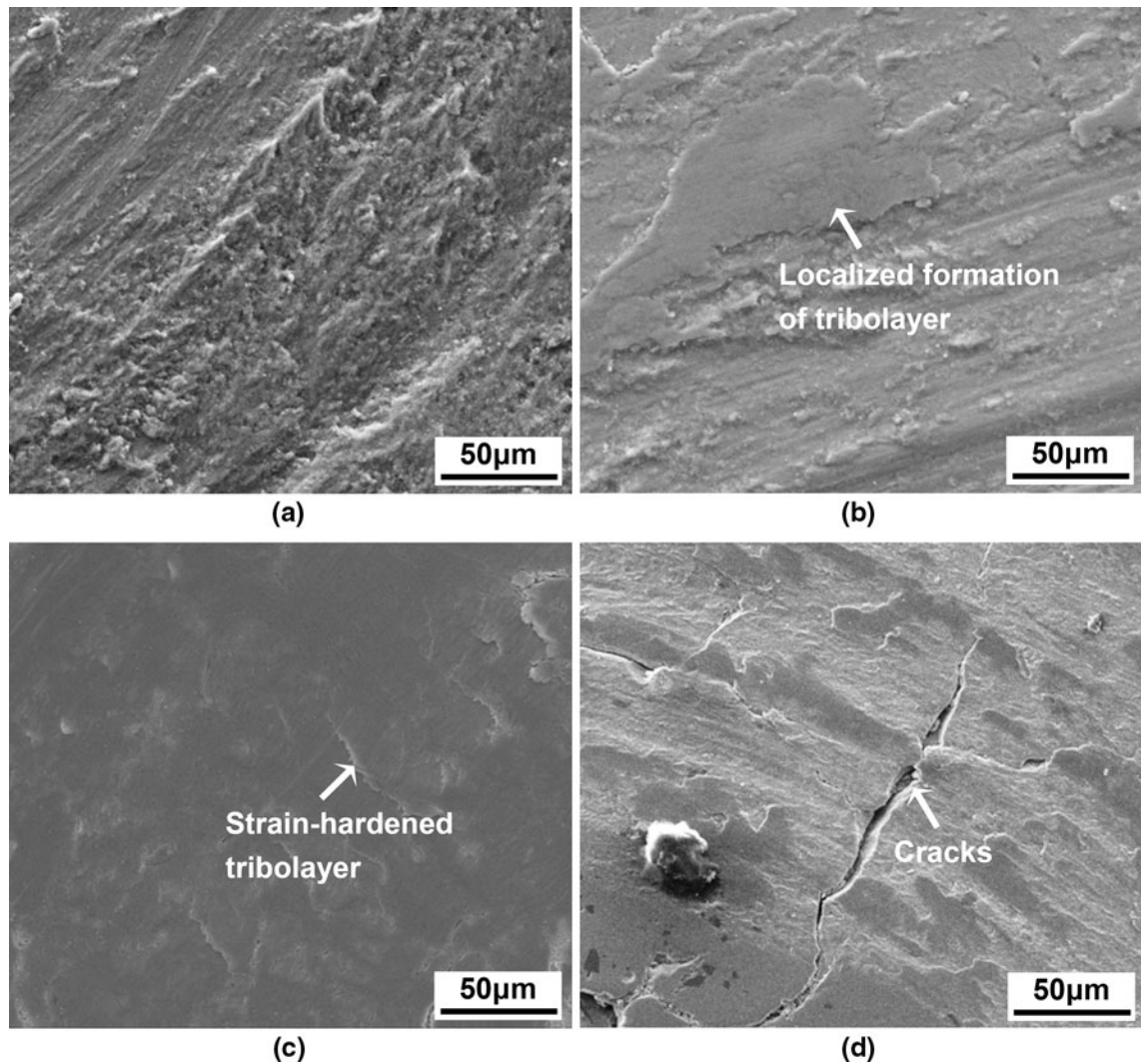
Fig. 12—SEM images showing characteristic morphologies of worn surfaces of SLM-processed composite parts at various laser energy densities (η): (a) $\eta = 2.5$ kJ/m; (b) $\eta = 3.33$ kJ/m; (c) $\eta = 5$ kJ/m; (d) $\eta = 10$ kJ/m.

IV. CONCLUSIONS

A novel SLM process was applied to prepare bulk-form *in situ* TiN/Ti$_5$Si$_3$ composites starting from Si$_3$N$_4$/Ti powder system. The main conclusions were summarized as follows:

1. The densification response of TiN/Ti$_5$Si$_3$ composite parts was controlled by the applied laser energy density. A combination of a low laser energy density (2.5 kJ/m) and a high scan speed (0.4 m/s) initiated the balling effect, whereas an excessive laser energy input (10 kJ/m) resulted in the thermal cracking. Both defects that were caused by an improper laser process control lowered the densification rate. A near-full 97.7 pct theoretical density was achieved as an optimal laser energy density of 5 kJ/m was settled properly.

2. The *in situ*-formed TiN reinforcing phase experienced a successive change in its morphologies: an irregular polyangular shape—a refined near-round shape—a coarsened dendritic shape, on increasing the applied laser energy density. The variations in the liquid–solid wettability and the intensity of Marangoni flow within the molten pool were responsible for the different growth mechanisms and morphologies of the TiN phase.

3. The optimally prepared TiN/Ti$_5$Si$_3$ composite parts had a uniform microhardness distribution with an increased mean value of 1358.0HV$_{0.3}$, showing at least a 4-fold increase on that of the unreinforced Ti. A considerably low friction coefficient of 0.19 without any apparent fluctuation and a decreased wear rate of 6.84×10^{-5} mm^3/Nm were obtained in sliding wear tests. The formation of adherent strain-hardened tribolayer covered on the worn surface accounted for the improvement of wear performance. However, the microhardness and wear resistance decreased at an excessive laser energy input because of the formation of thermal cracks and the significant coarsening of TiN dendritic reinforcement.

ACKNOWLEDGMENTS

REFERENCES

1. R. Mitra: *Metall. Mater. Trans. A*, 1998, vol. 29A, pp. 1629–41.
2. R. Mitra and V.V. Rama Rao: *Metall. Mater. Trans. A*, 1998, vol. 29A, pp. 1665–75.
3. J.H. Shim, J.S. Byun, and Y.W. Cho: *J. Am. Ceram. Soc.*, 2004, vol. 87, pp. 1853–58.
4. L.J. Wang, W. Jiang, C. Qin, and L.D. Chen: *J. Mater. Sci.*, 2006, vol. 41, pp. 3831–35.
5. I.J. Shon, H.C. Kim, D.H. Rho, and Z.A. Munir: *Mater. Sci. Eng. A*, 1999, vol. 269, pp. 129–35.
6. J.L. Li, D.L. Jiang, and S.H. Tan: *J. Eur. Ceram. Soc.*, 2002, vol. 22, pp. 551–58.
7. S.C. Tjong: *Adv. Eng. Mater.*, 2007, vol. 9, pp. 639–52.
8. A. Gåård, P. Krakhmalev, and J. Bergström: *J. Alloys Compd.*, 2006, vol. 421, pp. 166–71.
9. D.D. Gu, Y.C. Hagedorn, W. Meiners, K. Wissenbach R. Poprawe: *Surf. Coat Technol.*, 2011, vol. 205, pp. 3285–92.
10. J.F. Shackelford and W. Alexander: *CRC Materials Science and Engineering Handbook*, 3rd ed., CRC Press, Boca Raton, FL, 2000.
11. M.A. Thein, L. Lu, and M.O. Lai: *Mater. Sci. Eng. A*, 2010, vol. 528, pp. 239–46.
12. V. Abbasi Chianeh, H.R. Madaah Hosseini, and M. Nofar: *J. Alloys Compd.*, 2009, vol. 473, pp. 127–32.
13. C.L. Yeh and G.S. Teng: *J. Alloys Compd.*, 2007, vol. 429, pp. 126–32.
14. D. Horvitz and I. Gotman: *Acta Mater.*, 2002, vol. 50, pp. 1961–71.
15. Y.F. Yang, H.Y. Wang, J. Zhang, R.Y. Zhao, Y.H. Liang, and Q.C. Jiang: *J. Am. Ceram. Soc.*, 2008, vol. 91, pp. 2736–39.
16. S. Kumar, V. Subramaniya Sarma, and B.S. Murty: *Metall. Mater. Trans. A*, 2010, vol. 41A, pp. 242–54.
17. R. Hadian, M. Emamy, and J. Campbell: *Metall. Mater. Trans. B*, 2009, vol. 40B, pp. 822–32.
18. B. Zheng, T. Topping, J.E. Smugeresky, Y. Zhou, A. Biswas, D. Baker, and E.J. Lavernia: *Metall. Mater. Trans. A*, 2010, vol. 41A, pp. 568–73.
19. B. Zheng, J.E. Smugeresky, Y. Zhou, D. Baker, and E.J. Lavernia: *Metall. Mater. Trans. A*, 2008, vol. 39A, pp. 1196–205.
20. B.V. Krishna, S. Bose, and A. Bandyopadhyay: *Metall. Mater. Trans. A*, 2007, vol. 38A, pp. 1096–1103.
21. W.P. Liu and J.N. DuPont: *Metall. Mater. Trans. A*, 2005, vol. 36A, pp. 3397–406.
22. R. Banerjee, A. Genç, P.C. Collins, and H.L. Fraser: *Metall. Mater. Trans. A*, 2004, vol. 35A, pp. 2143–52.
23. J.P. Kruth, G. Levy, F. Klocke, and T.H.C. Childs: *CIRP Ann. Manuf. Technol.*, 2007, vol. 56, pp. 730–59.
24. D. Bourell, M. Wohlert, N. Harlan, S. Das, and J. Beaman: *Adv. Eng. Mater.*, 2002, vol. 4, pp. 663–69.
25. S. Das: *Adv. Eng. Mater.*, 2003, vol. 5, pp. 701–11.
26. A. Simchi, F. Petzoldt, and H. Pohl: *Int. J. Powder Metall.*, 2001, vol. 37, pp. 49–61.
27. S. Kumar and J.P. Kruth: *Mater. Des.*, 2010, vol. 31, pp. 850–56.
28. D.D. Gu and W. Meiners: *Mater. Sci. Eng. A*, 2010, vol. 527, pp. 7585–92.
29. D.D. Gu and Y.F. Shen: *Acta Metall. Sin.*, 2010, vol. 46, pp. 761–68.
30. D.D. Gu and Y.F. Shen: *J. Alloys Compd.*, 2009, vol. 473, pp. 107–15.
31. P. Fischer, V. Romano, H.P. Weber, N.P. Karapatis, E. Boillat, and R. Glardon: *Acta Mater.*, 2003, vol. 51, pp. 1651–62.
32. A. Simchi and H. Pohl: *Mater. Sci. Eng. A*, 2003, vol. 359, pp. 119–28.
33. Q.L. Huang, J. Cai, W. Pan, J. Chen, and J. Lian: *Mater. Lett.*, 1997, vol. 31, pp. 221–25.
34. I. Barin: *Thermochemical Data of Pure Substances*, 3rd ed., VCH, New York, NY, 1993.
35. D.D. Gu, Y.F. Shen, and Z.J. Lu: *Mater. Lett.*, 2009, vol. 63, pp. 1577–79.
36. K. Arafune and A. Hirata: *J. Cryst. Growth*, 1999, vol. 197, pp. 811–17.
37. X.B. Zhou and J.Th.M. De Hosson: *Acta Mater.*, 1996, vol. 44, pp. 421–26.
38. Z.F. Yuan, J.J. Ke, and J. Li: *Surface Tension of Metals and Alloys*, 1st ed., Science Press, Beijing, China, 2006.
39. I. Takamichi and I.L.G. Roderick: *The Physical Properties of Liquid Metals*, 1st ed., Clarendon Press, Oxford, UK, 1993.
40. H.J. Niu and I.T.H. Chang: *Scripta Mater.*, 1999, vol. 41, pp. 1229–34.
41. H.H. Zhu, L. Lu, and J.Y.H. Fuh: *Mater. Sci. Eng. A*, 2004, vol. 371, pp. 170–77.
42. P. Mercelis and J.P. Kruth: *Rapid Prototyping J.*, 2006, vol. 12, pp. 254–65.
43. B.S. Kim, S.J. Hong, and D.J. Kim: *Metall. Mater. Int.*, 2010, vol. 16, pp. 565–68.
44. K. Tsukuma, M. Shimada, and M. Koizumi: *Ceram. Bull.*, 1981, vol. 60, pp. 910–12.
45. M.F. Wani, Z.A. Khan, and M. Hadfield: *J. Adv. Res. Mech. Eng.*, 2010, vol. 1, pp. 52–59.
46. A. Jain, B. Basu, B.V. Manoj, K. Harshavardhan, and J. Sarkar: *Acta Mater.*, 2010, vol. 58, pp. 2313–23.